Received: Added at production | Revised: Added at production | Accepted: Added at production
DOI: xxx/xxxx

ARTICLE TYPE

Evaluation of Beamforming Strategies for Enhanced Space-Based Massive ADS-B Signal Detection

Xavier Artiga[1] | **Carlos Mosquera**[2] | **Roberto López-Valcarce**[2] | **Felipe Gómez-Cuba**[2] | **Pol Henarejos**[1]

[1]Centre Tecnològic de Telecomunicacions de Catalunya (CTTC-CERCA), Castelldefels, Spain
[2]atlanTTic Research Center, Universidade de Vigo, Spain

Correspondence
Corresponding author Xavier Artiga
Email: xavier.artiga@cttc.es

Abstract

This work proposes and evaluates beamforming techniques to enhance future LEO-based ADS-B reception targeting global coverage, including dense continental regions. An accurate interference model enables detailed characterization of interference conditions, revealing the detrimental impact of antenna sidelobe levels, particularly for aircraft operating in low-SNR regions. Combining amplitude tapering to reduce sidelobe effects with beam diversity achieved through oversampling at coverage edges yields consistent performance gains, which can be further enhanced by employing a Maximum a Posteriori decoder capable of resolving a single strong collision. Numerical simulations show that the achieved performance is scenario dependent. Across the considered scenarios, the proposed approach yields improvements of up to 49% in the proportion of aircraft satisfying a given position update interval probability, along with an effective coverage extension of up to 8°, compared to a standard uniform beam grid with –3 dB beam crossovers combined with basic decoder treating interference as noise, which already outperforms the conventional ADS-B receiver in the presence of ADS-B and Mode-S collisions.

KEYWORDS
ADS-B detection, LEO constellation, beamforming, beam diversity, tapering, effective coverage

1 | INTRODUCTION

Global air traffic is expected to continue growing over the coming decades, with passenger numbers projected to double compared to current levels by 2045, for a compound annual growth rate (CAGR) of 3.4% [1].This growth implies an increasing complexity and density in key flight corridors, which places greater emphasis on advanced surveillance technologies to ensure safety while reducing overall devoted infrastructure. Automatic Dependent Surveillance-Broadcast (ADS-B) has become a core technology solution, pushed by regulatory mandates around the world, such as those driven by the Federal Aviation Administration (FAA) [2] and the European Commission [3]. Unlike conventional radar, ADS-B relies on aircraft quasi-periodic broadcast messages of position, velocity, identification, and status information, providing air traffic controllers with improved situational awareness, enabling reduced separation and enhanced traffic flow in high-density airspace.

Terrestrial ADS-B systems depend on dense networks of ground receivers, which are inherently limited by geography and infrastructure availability. This results in significant coverage gaps over large oceanic expanses, polar regions, and remote land areas where ground stations are impractical. Space-based ADS-B consisting of the reception of the standard ADS-B broadcasts by Low Earth Orbit (LEO) satellites, addresses this critical limitation by providing near-global surveillance coverage [4]. Aireon [5,6], with payloads hosted in Iridium Next satellites, pioneered space-based ADSB commercial services, subsequently being followed by other initiatives including Spire or Startical [7].

The performance of Air Traffic Systems (ATS) surveillance is regulated by organizations such as EUROCAE [8]. An essential requirement is the probability of receiving a position message update within a specified interval, which EUROCAE sets at 95% or higher for an interval of 5 to 8 seconds, depending on the specific operational scenario. The primary challenge to meet it lies in the uncoordinated nature of ADS-B message transmissions from different aircraft, which results in an interference-limited system with a high collision probability, especially considering that the satellites field of view (FoV) can simultaneously cover thousands of aircraft. Indeed, large FoV are desired to reduce the total number of satellites required to provide global coverage. Moreover, in addition to ADS-B, the 1090 MHz band is also shared with Mode-S and Mode A/C reply signals [9], triggered by secondary surveillance radar (SSR), further increasing probability of collision. The ADS-B standard issued by the International Civil Aviation Organization (ICAO) [10] addresses this challenge by employing transmission time diversity, randomizing the exact transmission time of each message to reduce the likelihood of collisions. Besides, it requires category 1, 2, and 3 receivers to perform at least as well as the multi-sample technique benchmark described in the appendix of the DO260B Minimum Operational Performance Standards (MOPS) document [11], which mitigates interference during symbol detection using preamble-based amplitude estimation.

Two main approaches have been proposed to enhance the reception performance beyond the baseline standard. On the one hand, advanced signal separation algorithms that can distinguish and recover ADS-B messages even when multiple signals collide at the receiver. They include interference cancellation and projection-based suppression like iterative time-domain cancellation [12] and orthogonal projection linearly-constrained minimum variance (OPLCMV) [13]; time/frequency and statistical separation exploiting differences in arrival time, Doppler, or non-Gaussian properties to recover colliding transmissions, like minimum dispersion criterion methods [14]; and data-driven approaches employing deep neural networks such as temporal convolutional networks or recurrent architectures to separate overlapping signals directly from waveforms [15,16].

On the other hand, directional antennas or beamforming arrays allow reducing the effective FoV, permitting the receiver to spatially isolate signals and mitigate collisions. Current solutions include a multichannel concept with four antennas pointing to different sectors aiming small satellites [4] or a more capable 3D array structure synthesizing seven fixed beams [17]. These fixed beamforming architectures however become inefficient since they cannot adapt to changing aircraft distributions. Moreover, they may not be able to cope with the air traffic increase or the traffic density out of oceanic areas due to the small number of beams/sectors. Indeed, Aireon payload uses a similar 3D array structure but it can synthesize up to 62 beams (with plans to increase it up to 80), 20 of them simultaneously [7], which suggest the use of some sort of reconfiguration to adapt to different distributions.

Still, full adaptability to air traffic distribution dynamically adjusting beam patterns to concentrate gain over regions of high aircraft density requires digital adaptive beamforming. Proposed techniques in this direction include global heuristic optimization like genetic algorithms [18], cooperative coevolution [19], or machine learning approaches [20]. However, global optimization is computationally demanding and machine learning approaches shift the complexity to the training phase, which must be wide enough to represent all possible scenarios. Moreover, these references do not accurately model the signal and interference levels coming from different aircraft. Yu *et al.* [18] model the probability of detection (P_d) per beam as a function of the number of aircraft exceeding the receiver sensitivity in that beam, thus artificially equaling the P_d of all aircraft covered by the same beam. The P_d model of Li *et al.* [19] depends on the signal-to-noise ratio (SNR) at aircraft level and on the probability of signal collision, which again considers the number of aircraft but no the interference levels different aircraft in different position can cause. Xiang *et al.* [20] do not describe in-depth their P_d model but fix a bit error rate of 10^{-3}, not depending on signal-to-interference-plus-noise-ratios (SINR). Other limitations of these works are their decoder model, which does not tolerate any collision with ADS-B or Mode-S signals, and the use of a fixed number of beams that is much lower than those used in a commercial system like Aireon (only Yu *et al.* [18] provide results for an increased number of beams up to 33). Finally, their global optimization approach does not provide physical insights on the interference patterns, e.g., the role of sidelobe levels or the behavior at coverage edges.

This study proposes and evaluates beamforming strategies for next-generation LEO-based ADS-B systems aimed at global operation independent of terrestrial infrastructure, i.e., capable of meeting performance requirements even over densely populated continental regions. In contrast to the previous works, the considered architecture relies on satellites with large field of view limited only by the Earth's horizon, thereby minimizing the number of satellites required for global coverage. To support this demanding scenario, an enhanced ADS-B payload is assumed, supporting several hundred synthesized beams generated by a 1 m^2 planar digital beamforming antenna. In contrast to some existing literature like studies included in the ITU report [9, Annex 6] or the work by Yu *et al.* [18], we also investigate the impact of transmissions from both the top- and bottom-mounted aircraft antennas. This introduces a tradeoff between the additional diversity provided by the two antennas and the increased message rate, which results in higher probability of collision. Particular emphasis is placed on the simulation framework, which evaluates the SINR at bit level by accounting for the beam pattern as well as the position and transmit power of all active transmitters at each time instant. The resulting SINR values are mapped to detection probabilities through the physical-layer abstraction of two advanced receiver models that outperform the DO-260B standard under ADS-B and/or Mode-S collision conditions: a Treating Interference as Noise (TIN) decoder, which is optimal in additive white Gaussian noise channels, and a proposed Maximum A-Posteriori (MAP) decoder capable of mitigating the impact of a dominant interferer. This modeling enables an in-depth characterization of interference, revealing the negative impact of high sidelobe levels and that the combination of low SNR regions and high traffic load constitutes the most challenging conditions for achieving the required update interval probability. Based on these findings, we propose a combination of amplitude tapering and beam diversity to increase the effective coverage area satisfying a given update interval probability, without the need of resorting to computationally complex global optimizations. Besides, null-steering and distributed sparse arrays are qualitatively discussed and discarded.

Preliminary results of this study were included in a recent conference contribution[21], which is extended herein by providing an in-depth description of the system and simulation model including the abstraction of the two decoders; the evaluation of a more challenging scenarios; the comparison of different amplitude tapering windows; the smart combination of beam over and under sampling to increase effective coverage while keeping a reasonable number of beams; the assessment of the combination of beamforming techniques with the two decoder models; the qualitative discussion on alternative null-steering and sparse array techniques; and the impact of considering transmissions from both top- and bottom-mounted aircraft antennas.

The remainder of document is organized as follows. Section 2 details the system description and Section 3 presents the physical abstraction of TIN and MAP decoders. Section 4 presents the interference characterization over a baseline grid of fixed beams and introduces the proposed beamforming techniques, which are numerically evaluated in Section 5. Finally, conclusions are presented in Section 6.

2 | SYSTEM DESCRIPTION

2.1 | ADS-B signal model

ADS-B transmissions consist of short, fixed-length packets broadcast in an uncoordinated and asynchronous manner in the 1090 MHz frequency band. Each packet has a total duration of 120 μs and comprises a known preamble followed by a 112-bit data payload, referred to as the extended squitter (ES). The preamble occupies the first 8 μs and enables packet detection, synchronization, and amplitude estimation at the receiver. The payload encodes aircraft state information following ICAO specifications. The signal modulation used in 1090ES ADS-B is pulse-position modulation (PPM) with a symbol duration of 1 μs, where each data bit is conveyed by the position of a 0.5 μs pulse, resulting in a raw data rate of 1 Mbps.

Several types of ADS-B messages are transmitted quasi-periodically, each with a specific update rate. Position messages, which include latitude, longitude, and altitude, are typically broadcast at 2 messages per second. Velocity messages, conveying ground speed, vertical rate, and track angle, are usually transmitted at 1 message per second. Identification messages, containing the aircraft call sign, are broadcast every 5 seconds, and additional status or operational messages may be transmitted at lower rates depending on aircraft dynamics. To reduce the probability of collisions on the 1090 MHz channel, the exact transmission instant of each message is randomized within its nominal interval. For instance, position messages are transmitted at uniformly distributed instants within a time window ranging from 0.4 s to 0.6 s after the previous transmission. Most transponders implement antenna diversity, with separate antennas mounted on the top and bottom of the aircraft, with packet transmissions alternating between these antennas.

In addition to ADS-B, aircraft respond to Mode S interrogations from ground radar or other aircraft. Mode S replies occupy the 1090 MHz channel with two principal durations: short replies, corresponding to 64 μs of channel occupancy, and long replies, including extended squitters, corresponding to 120 μs. Unlike ADS-B, Mode S replies are initiated by interrogation pulses, so their timing is stochastic and depends on the interrogation rate. Replies are transmitted through the antenna (either top or bottom) that received the interrogation with more signal strength. Mode A/C short replies, triggered by Secondary Surveillance Radar (SSR) interrogations, also operate in the 1090 MHz band. However, these transmissions correspond to legacy surveillance systems that are being progressively phased out.

A key performance metric of the ADS-B system is the probability of update interval ($PUI(T)$), defined as the probability of having at least one successful detection of a position message within a time interval of length T. The required performance is regulated by EUROCAE[8], which set the requirement to $PUI(T) \geq 95\%$ for $T = 5$ s or $T = 8$ s, depending on the specific conditions.

2.2 System model

We consider a single LEO satellite equipped with an ADS-B receiver payload as the fundamental building block of a larger constellation. The satellite operates at a fixed orbital altitude and provides coverage over a time-varying set of aircraft distributed over the Earths surface. The instantaneous service region is defined by the satellite field-of-view (FoV), determined by geometric visibility and the antenna radiation pattern.

Due to the spherical geometry of the Earth, a locally uniform spatial distribution maps into a non-uniform angular density, leading to an increased concentration of users at higher off-nadir angles. This effect, combined with antenna gain degradation at large scan angles, limits the achievable quality of service near the FoV boundaries.

We define the effective coverage as the subset of the FoV where the required service level is met for a specified fraction of aircraft, in terms of the probability of update interval (PUI). The objective of this work is to maximize this effective coverage under the considered constraints, thereby increasing the fraction of traffic that can be served at acceptable performance levels.

From a constellation design perspective, the number of satellites required for continuous global coverage is driven by the coverage footprint of each satellite. Hence, enlarging the effective coverage of an individual satellite reduces the required spatial and temporal overlap between satellites, ultimately decreasing the number of satellites needed to ensure uninterrupted global service under standard geometric coverage assumptions.

Fig. 1 illustrates a ADS-B digital beamforming payload architecture. It consists of a digital beamformer antenna synthesizing multiple simultaneous beams followed by a parallel processing of each beam including preamble detection, data demodulation and CRC verification. Since the focus of this work is on digital beamforming design and its performance when combined with either a standard decoder or an advanced decoder capable of resolving a single collision, perfect preamble detection is assumed. Although this assumption yields an optimistic model of the satellite service, it enables a direct fair comparison of the considered beamforming schemes under the two decoding strategies. Accordingly, the performance results should be interpreted in terms of relative improvements with respect to the benchmark scenario rather than in absolute terms.

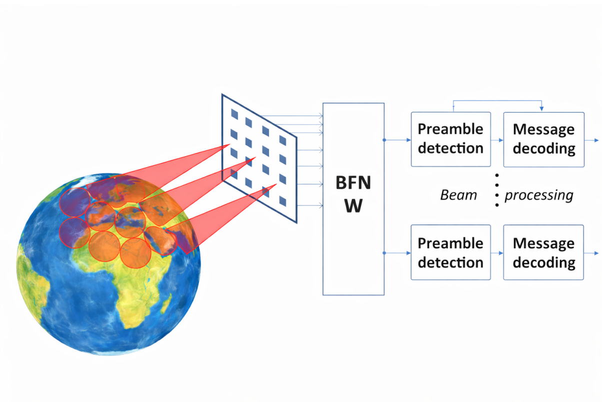

FIGURE 1 ADS-B receiver payload.

Let us consider a digital antenna with K radiating elements forming B simultaneous beams to cover a targeted FoV containing N aircraft. A pulse transmitted by aircraft n is received in beam b with power

$$R_{bn} = P_{tx}|\mathbf{w}_b^H \mathbf{h}_n|^2, \tag{1}$$

where P_{tx} denotes the peak RF transmit power of the aircraft transponder during pulse transmission, $\mathbf{w}_b$ is the beamforming vector of beam b, and $\mathbf{h}_n = \begin{pmatrix} h_{n1} & \cdots & h_{nK} \end{pmatrix}^T$ is the channel vector of aircraft n. The coefficients of this vector are calculated as

$$h_{nk} = \sqrt{\frac{G_{tx}(\theta_a)\, G_e \cos^2\theta_s\, \lambda^2}{(4\pi r_n)^2} OL}\; e^{-j\frac{2\pi}{\lambda}(x_k u + y_k v)}, \tag{2}$$

where G_{tx} is the gain of the aircraft antenna; G_e is the gain of the receiving element on the satellite antenna and $\cos^2\theta_s$ is its radiation pattern model; θ_s and θ_a are the scan angles in which the satellite sees the aircraft and the aircraft see the satellite, respectively; λ is the wavelength, r_n is the distance between the satellite and aircraft n, x_k and y_k denote the position of the k-th element of the array, and (u, v) is the angular position of aircraft n. OL refers to other losses such as depolarization, ionospheric, tropospheric, implementation, etc.

The corresponding SNR in linear scale for a pulse transmitted by aircraft n and received in beam b is then

$$\mathrm{SNR}_{bn} = \frac{R_{bn}}{K_B T Bw}, \tag{3}$$

where K_B is Boltzmann's constant, T the equivalent noise temperature of the receiver, and Bw the signal bandwidth. Due to the uncoordinated nature of ADS-B transmissions and the channel sharing with Mode-S replies, the message sent by aircraft n may collide with one or multiple messages sent by other aircraft. The resulting SINR in linear scale for a pulse transmitted by aircraft n and received in beam b in presence of C pulse collisions is calculated as

$$\mathrm{SINR}_{bn} = \frac{SNR_{bn}}{\sum_{c=1}^{C} SNR_{bc} + 1}. \tag{4}$$

The probability of successful message detection P_d depends on the SINR value through the entire message duration and on the detector used. Section 3.1 provides an abstraction model of the two detectors considered in this paper, based on the evaluation of the SINR expression on different message segments. Knowing the probability of detection Pd of each message s, the update interval probability $PUI(T)$ of position messages can be calculated as

$$PUI_{bn}(T) = 1 - \prod_{s=1}^{S} (1 - Pd_{bn}(s)), \tag{5}$$

where $S = \lfloor T r_m \rfloor$ is the number of message detection occasions in the update interval T for a message transmit rate of r_m. Since detection may happen simultaneously in multiple beams, the total update interval probability for aircraft n writes as

$$PUI_n(T) = 1 - \prod_{b=1}^{B} (1 - PUI_{bn}(T)). \tag{6}$$

2.3 | Proposed scenario

We consider a next-generation space-based ADS-B system designed to provide global services, including coverage of densely populated continental regions, in a fully autonomous manner without reliance on terrestrial receivers. Our objective is to maximize the effective coverage of a single satellite, defined as the region where the required probability of update interval is achieved for a specified percentage of aircraft. Expanding the coverage of an individual satellite consequently reduces the total number of satellites needed for global coverage. These requirements present significant operational challenges that exceed those of current commercial missions, such as Aireon, due to high traffic densities in continental regions. Such densities become even larger when observed at large scan angles. To address this challenge, we assume enhanced payload capabilities, including an increased, yet practical, antenna size of 1 m^2. This corresponds to an 8×8 planar array of microstrip patch-like radiating elements, modeled with a gain of 5.5 dBi and a $\cos^2 \theta_s$ radiation pattern, as described in the previous section. To fully exploit the increased antenna size, we also consider increasing the number of simultaneous beams by up to one order of magnitude with respect to current commercial missions[7]. The computational load scales approximately linearly with the number of simultaneously processed beams due to both the digital beamforming operations and the independent signal processing and decoding required for each beam. The resulting increase in computational complexity can be justified by the substantially larger coverage area assigned to each satellite, which may enable a reduction in the number of satellites required to provide continuous global coverage. In this context, the proposed architecture trades increased onboard processing complexity for a reduced constellation size while enabling improved ADS-B message reception performance in high-air-traffic-density scenarios. A detailed payload feasibility assessment, including processing, power, thermal, and mass budgets, is beyond the scope of this work.

Table 1 summarizes the system parameters used in the remainder of this paper, unless otherwise stated. The probability of update interval requirement is set to 95% for an interval of $T = 8$ s, which is the reference used to evaluate the update interval from Aireon data[22]. Aircraft transponder transmit power is set according to ITU report[9]. Additional losses include a 3 dB polarization loss, 0.5 dB ionospheric loss, and an implementation loss of 0.2 dB. System performance strongly depends on the offered load, determined by the message transmission rate per aircraft and the assumed aircraft antenna patterns. Some available literature, as identified in the introduction, assume that only messages transmitted by the top-mounted antenna are received by the satellite, neglecting transmissions from the bottom-mounted antenna. This assumption cannot be adopted here because the large field of view (FoV) considered for each satellite may result in comparable top- and bottom-antenna gains at low elevation angles. Moreover, practical aircraft antenna patterns deviate significantly from ideal monopole patterns due to the aircraft airframe. The measured top-antenna pattern reported in the ITU report[9, p. 5] exhibits substantial gain variations beyond the theoretical null along the monopole axis; however, no corresponding measurements are provided for the bottom antenna. To assess the impact of practical antenna patterns, we therefore assume the measured ITU pattern for both antennas. The corresponding gain patterns are shown in Fig. 2. Gains are not only comparable at low elevations (θ=90°) but also at high elevations. Remarkably around θ=30° the bottom antenna may provide larger gain.

Two traffic scenarios are considered. The first includes only top-antenna transmissions, with 3 ADS-B messages/s and 6 Mode-S replies/s per aircraft. The second includes transmissions from both antennas, with 3 ADS-B messages/s per antenna and 6 Mode-S replies/s randomly assigned to either the top or bottom antenna. Mode A/C transmissions are neglected, as they are being progressively phased out.

TABLE 1 System parameters

Parameter	Value/description
Transponder power distribution	125 W (25%) 250 W (50%) 500 W (25%)
ADS-B Message rate	3 messages/s/antenna
Mode-S Message rate	6 messages/s (through either top antenna or randomly on top and bottom antennas)
Aircraft antenna	As per ITU report[9, p. 5]
Satellite Antenna	8×8 array, $\lambda/2$ separation (1 sqm)
Antenna element gain	5.5 dBi
Antenna element radiation pattern	$\cos^2\theta$
Receiver bandwidth	2 MHz
Receiver noise temperature	500°K
Number of beams	100-200
Satellite orbit height	550 km
Frequency	1090 MHz
Additional losses	3.7 dB

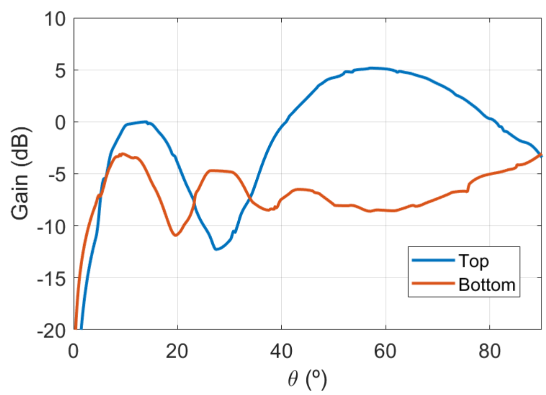

FIGURE 2 Aircraft antenna radiation patterns

3 | DETECTOR MODEL

In the ADS-B frame, the data following the preamble is modulated via binary orthogonal PPM with bit interval $T_b = 1\ \mu$s. The $N_b = 112$ bit message $b_0, b_1, \ldots, b_{N_b-1}$ with period T_b is represented by rectangular pulses (AKA "chips") with duration $T_c = T_b/2$. We assume the received signal is frequency downconverted for each single beam and digitally oversampled with rate $1/T_s = M/T_c$ samples/s, i.e., taking M samples per chip. Samples can be either complex (coherent receiver via IQ demodulation) or real positive (non-coherent receiver via envelope detection). To design the demodulator we assume that timing, signal amplitude, phase and carrier frequency offset (CFO) of the desired signal have been perfectly estimated from the preamble and subsequently compensated. We write the received signal samples for bit b_n during period nT_b as

$$\mathbf{r}_n = \mathbf{s}_{b_n} + \mathbf{a}_n + \mathbf{z}_n \quad \text{where} \quad \mathbf{s}_{b_n} = \begin{cases} (1, \overset{\times M}{\cdots}, 1, 0, \overset{\times M}{\cdots}, 0)^T & \text{if } b_n = 1, \\ (0, \overset{\times M}{\cdots}, 0, 1, \overset{\times M}{\cdots}, 1)^T & \text{if } b_n = 0, \end{cases} \tag{7}$$

with $\mathbf{s}_{b_n}$ being the ideal transmitted signal samples as a function of bit b_n, $\mathbf{a}_n$ are the interference samples with an arbitrary distribution $f(\mathbf{a})$, and $\mathbf{z}_n$ are the AWGN noise samples. While $\mathbf{s}_{b_n}$ is normalized, $f(\mathbf{a})$ must model the amplitude difference and time offset between the interference and the desired signal. In the coherent case, $f(\mathbf{a})$ must also model the phase and CFO offset between the interference and the desired signal. For the definitions of SNR (3) and SINR (4) to remain consistent in this normalized discrete channel, using $\mathsf{SNR} = \frac{\mathbb{E}[\|\mathbf{s}_{b_n}\|^2]}{\mathbb{E}[\|\mathbf{z}_n\|^2]} = \frac{M}{2M\sigma^2}$ we set the normalized noise variance to $\sigma^2 = \frac{K_B T \frac{2M}{T_b}}{2R_{bn}}$, and the normalized Interferece to Signal Ratio (ISR) defined as $\frac{\mathbb{E}[\|\mathbf{a}_n\|^2]}{\mathbb{E}[\|\mathbf{s}_{b_n}\|^2]} = \frac{\mathbb{E}[\|\mathbf{a}_n\|^2]}{M} = \frac{SNR_{bc}}{SNR_{bn}}$ is taken into account in the distribution $f(\mathbf{a})$.

The goal of the detector is to decide the value of the transmitted bit $\hat{b}_n$, given the channel observation $\mathbf{r}_n$. To that end, we distinguish three receiver schemes:

- The **Treating Interference as Noise (TIN)** scheme is the optimal receiver in AWGN channels[23], where the Maximum Likelihood, the Nearest Symbol in Euclidean distance, and the correlation-based receivers are equivalent:

$$\hat{b}_n^{\mathsf{TIN}} = \arg\min_{b_n} \|\mathbf{r}_n - \mathbf{s}_{b_n}\|^2 = \arg\max_{b_n} 2\Re\{\mathbf{s}_{b_n}^H \mathbf{r}_n\} + \text{constants} \tag{8}$$

  The name TIN stems from the fact that this receiver would be optimal if $\mathbf{a}_n$ was Gaussian distributed with variance equal to the interference power. In that case, the BER of this receiver would correspond exactly to the expression $Q(\sqrt{M\ \mathrm{SINR}})$. In this expression we consider the full system bandwidth noise power in the SINR, not the projection of the noise into the signal subspace by the correlator (8), and the noise equivalent bandwidth in (3) grows with M, making the product $M \cdot \mathrm{SINR}$ remain constant when M increases. This result means that the error with AWGN does not depend on M). While this technique suffers the shortcoming of being suboptimal when the interference is significantly different from a Gaussian, its use (in correlation implementation form) has been proposed in[24] in combination with an advanced Cyclic Redundancy Check (CRC) Forward Error Correction (FEC) "$\{a, b\}$ algorithm", as it offers advantages in space-based ADS-B systems where the interference is the sum of many weak collisions (closer to a Gaussian by CLT). Since there are two bit pulses represented by vectors of size $2M$, this detector requires $4M$ floating point multiplications per decoded bit.
- The **DO-260B** multi-sample technique specified in the standards[11,25] is capable of successfully making decisions on bits suffering strong Mode AC collisions in a non-coherent envelope receiver. This is done by counting how many of the M samples per chip are at the preamble level ±3dB and how many are below the preamble level –6dB[26,27]

$$\begin{aligned} C_{H1} &= \text{no. of samples of chip 1 with preamble energy} \pm 3\text{ dB}, \\ C_{L1} &= \text{no. of samples of chip 1 below preamble energy} - 6\text{ dB}, \\ C_{H0} &= \text{no. of samples of chip 0 with preamble energy} \pm 3\text{ dB}, \\ C_{L0} &= \text{no. of samples of chip 0 below preamble energy} - 6\text{ dB}, \end{aligned}$$

$$\hat{b}_n^{\mathsf{DO\text{-}260B}} = \begin{cases} 1 & \text{if } C_{H1} + C_{L0} > C_{H0} + C_{L1}, \\ 0 & \text{if } C_{H1} + C_{L0} \leq C_{H0} + C_{L1}. \end{cases} \tag{9}$$

  This technique has two shortcomings: First, the standard specification is defined in magnitude, as in classic non-coherent receivers, and there is no indication on how to perform this technique in the coherent case. And secondly, the multi-sample technique was designed to combat Mode AC collisions, but it does not mitigate the interference of Mode S collisions which dominate space-based ADS-B scenarios and still produce 100% packet loss probability according to the performance model in[5]. In general the multi-sample technique is regarded as a better receiver than TIN for legacy ground ADS-B systems, when the receivers were non-coherent and Mode AC collisions were predominant. The DO-260B receiver can label the bits "confidence" for later use by CRC FEC algorithms. In the literature, this bit declaration technique is used ahead of CRC FEC schemes such as the originally proposed polynomial syndrome method[28] or the brute-force search method[26]. Due to the use of a square sample magnitude, if this receiver starts from coherent baseband IQ samples this technique requires 2 complex floating point multiplications for a total of $4M$ as well. The complexity can even be lower if samples at the output of an energy detector log-amp are readily available.

- The **Maximum A-Posteriori (MAP)** decision scheme is the minimum error probability of error receiver when the probability density function interference vector $\mathbf{a}_n$ is known. This expression can generalize the optimal receiver for an AWGN channel by finding the maximum of the likelihood function of the channel output written as

$$\hat{b}^{\mathsf{MAP}} = \arg\max_b \mathcal{L}_{\mathbf{r}}(b) = \arg\max_b f(\mathbf{r}|b) = \arg\max_b \int f(\mathbf{r}|b, \mathbf{a}) f(\mathbf{a}) d\mathbf{a}. \tag{10}$$

The name MAP stems from the fact that to implement this receiver we need to calibrate the a-priori distribution $f(\mathbf{a})$ and update the results for the conditional distribution $f(\mathbf{r}|b, \mathbf{a})$ with it, like Turbo and LDPC decoding algorithms do. In our experiments, we verified that *a*) the DO-260B scheme is a particular case of the MAP scheme calibrated to Mode AC collisions in a non-coherent receiver, by assuming a distribution $f(\mathbf{a})$ modelled after a single large Mode AC collision pulse. In this case, the integral (10) is approximated numerically with an a-priori distribution representing all possible clock offsets of the interference Mode A/C pulse $\tau_{\text{ModeA/C int.}} \sim U(-0.45, +1)\mu s$ which is approximated by a quantization with a grid of size $3M$. Even though the signals are simulated with CFO, the `abs()` operation of the envelope detector removes the need to consider CFO in the integral. Thus every value in the numerical sum approximation of the integral (10) requires two additional correlations of vectors of size $2M$, making the total complexity of the receiver $O(4M+4M^2)$. And *b*) by calibrating $f(\mathbf{a})$ in MAP scheme to model a single large Mode S collisions in a coherent receiver, we can significantly outperform the BER of both TIN and DO-260B receivers for space-based ADS-B systems where the assumption of predominant Mode S collisions and coherent hardware holds. By exploiting its relations to the TIN and DO-260B schemes, the MAP scheme can be coupled with all existing CRC FEC algorithms in the literature as well[28,26,24]. In this case, the integral (10) is approximated numerically with an a-priori distribution representing all possible clock offsets of the interference Mode S bit boundary $\tau_{\text{ModeS int.}} \sim U(0, +1)\mu s$, and four previous and next bit transitions at this boundary. Moreover, the coherent receiver retains the interference CFO in the distribution. Thus the integral is approximated by a quantization with a grid of size $2M$ plus an FFT of the same dimensions to evaluate the interference CFO, times a factor of four to account for all possible interference bit pulse cases before and after the clock offset boundary. Thus every value in the numerical sum approximation of the integral (10) requires $O(4M + 32M^2 \log(2M))$ operations. The details about the MAP receiver implementation are beyond the scope of this article, and can be found in the work from Gómez-Cuba *et al.*[29]

We depict the BER for 10^5 i.i.d. Monte-Carlo single-bit pulse decoding simulations if Fig. 3. The simulation is conducted with a single strong collision with probability 40%. We compare non-coherent receivers with predominant Mode AC collisions (legacy radio hardware on land scenario) and coherent receivers with predominant Mode S collisions (next gen ADS-B roadmap and satellite scenario). In both cases, the desired signal pulse $\mathbf{s}_{b_n}$ in (7) is simulated with perfect frequency and timing synchronization. The main motivation to design the bit decoder assuming perfect symbol timing offset and CFO for the desired signal is the fact that the DO-260B receiver is also specified under the assumption of perfect preamble detection. With regard to interference, in our simulations all interfering signals were generated with nominal phase ($U(0, 2\pi)$), CFO ($U(-100, 100)$ kHz) and timing synchronization errors relative to the desired bit ($U(-0.45, +1)\mu$s for Mode A/C and $U(0, 1)\mu$s for Mode S). All simulations were conducted under nominal impairments for interference for all cases. In the Non-Coherent case, the signal is generated **with** phase and CFO offsets and passed through an `abs()` block before bit decision, and hence the interference CFO is present in the channel but goes away and the MAP receiver numerical integral does not need to evaluate its distribution. Note that all schemes under interference perform much worse than the AWGN case given by $\mathcal{Q}(M\ \text{SNR})$. In the non-coherent case with Mode AC collisions, the TIN scheme performs close to $\mathcal{Q}(\sqrt{M\ \text{SINR} - 3dB})$, where the $-3dB$ penalty is due to the doubling of noise power with an envelope detector. The DO-260B scheme significantly outperforms the TIN receiver in this case, and the MAP scheme reproduces the advantages of the DO-260B scheme, even with some improvement. On the other hand, in the case of Mode S collisions with an IQ coherent receiver, the TIN receiver performs almost exactly as $\mathcal{Q}(\sqrt{M\ \text{SINR}})$

thanks to the reduction of noise in the coherent receiver, and the DO-260B scheme performs very poorly due to the fact that its design was conceived to mitigate Mode A/C interferences rather than Mode S. Finally, the MAP scheme with the a-priori interference distribution correctly calibrated to the satellite ADS-B scenario assumptions achieves a substantial improvement in the BER at the cost of a substantial, but still polynomial, increase in complexity.

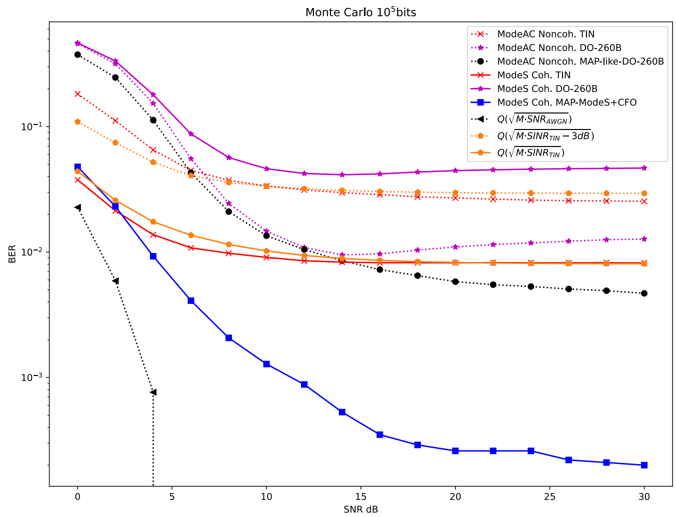

FIGURE 3 ADS-B PPM single-bit data demodulation BER comparison.

3.1 | Abstraction model

To avoid fully simulating bit modulation and decoding in the presence of noise, we calibrate a link abstraction model able to represent partially overlapping ADS-B collisions by knowing only the times of arrival and signal powers of each of the signals. We write the probability of reception for each ADS-B packet as $P_R = P_{M|P}P_P$, where P_P is the probability of preamble detection and $P_{M|P}$ is the probability of successful 112 bit message decoding. In our abstraction we assume a perfect preamble detection and provide a characterization of $P_{M|P}$.

The desired signal spans in time from $t \geq 0$ to $t \leq T_{ADSB} = 112\mu$s and has power P_S. It is contaminated by N_{col} collisions, however not all collisions are present in all time instants. We denote the start time of each interfering signal and its power as $\tau_i \in [-T_{preamble} - T_{ADSB}, T_{ADSB}], P_I^{(i)}\ \forall i \in \{1 \dots N_{col}\}$. We provide an example representation of the interference arrival process in Fig. 4.

The successful message decoding requires 112 independent successes in 112 independent bit decoding attempts with **non-identically** distributed success probabilities. We define a **packet segment** $\mathcal{S}_s$ as each of the maximum intervals of time within the packet that have all bits of equal decoding error probability $P_e^{(s)}$. The boundaries between the segments can take place in any collision arrival or end instant $\{\tau_i\}_{i=1}^{N_{col}} \cup \{\tau_i + 120\mu s\}_{i=1}^{N_{col}}$. Each segment is characterized by three parameters: its start time τ_s, its length in bits L_s, and the set of present collisions $\mathcal{P}_s \subset \{1 \dots N_{col}\}$.

The PHY abstraction is built by following three steps: 1) Divide the full packet in time segments $\{\mathcal{S}_s\}_{s=1}^{N_S}$. 2) Compute $P_e^{(s)}$ for each segment as a function of $\mathcal{P}_s$, P_S, $P_I^{(n)}$ and the noise power σ_z^2. 3) Evaluate the message decoding probability as a generalized 112-attempts non-uniform Binomial distribution $P_{M|P} = \prod_{s=1}^{N_S}(1 - P_e^{(s)})^{L_s}$

For the TIN receiver, as we have seen the BER is well characterized by $Q(\sqrt{M}\ \text{SINR})$. Moreover, other receiver algorithms can remove "up to a certain point" the interference of **one strong interferer**, but they behave nearly like TIN in the case of

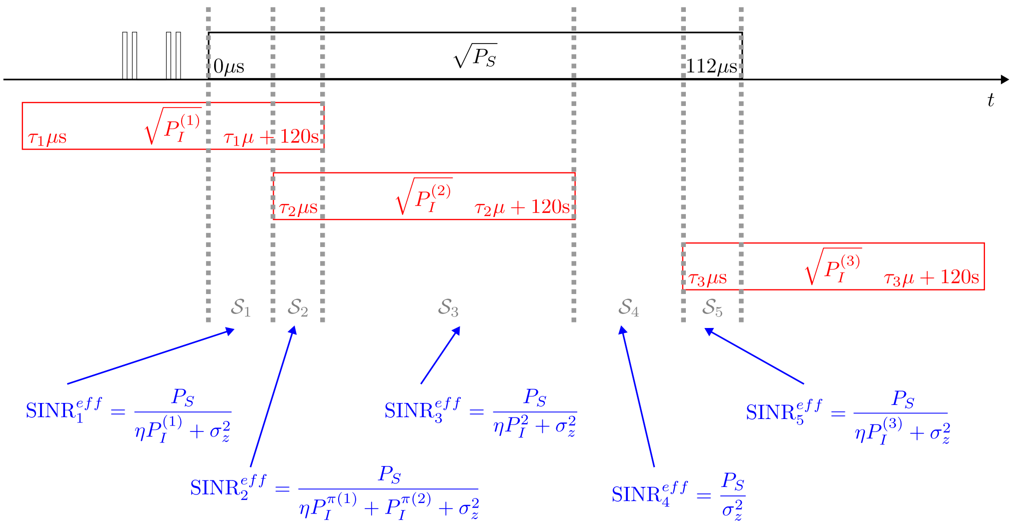

FIGURE 4 PHY abstraction: illustration with five segments.

many weak collisions. Therefore, we define the *interferer index sorting permutation* as

$$\pi(n) : \{1 \dots |\mathcal{P}_s|\} \to \mathcal{P}_s \quad \text{s.t.} \quad P_I^{\pi(n)} > P_I^{\pi(n+1)} \;\; \forall n.$$

Also, we define the *interference residue coefficient* $\eta \leq 1$ as the remaining relative power of the single largest collisions. This calibration coefficient must be set for each receiver algorithm. Combining the above, we model the *effective SINR* and the BER of segment s for any receiver with residue coefficient η as

$$P_e^{(s)} = Q\left(\sqrt{M \cdot \text{SINR}_s^{eff}}\right) \text{ where } \text{SINR}_s^{eff} = \frac{P_S}{\eta P_I^{\pi(1)} + \sum_{n=2}^{|\mathcal{P}_s|} P_I^{\pi(n)} + \sigma_z^2}. \tag{11}$$

An example evaluation of the effective SINRs for a case with five segments is given in Fig. 4.

Denoting the Interference to Signal and Noise Ratio (ISNR) $\gamma_I = \frac{P_I^{\pi(1)}}{P_S + \sum_{n=2}^{|\mathcal{P}_s|} P_I^{\pi(n)} + \sigma_z^2}$. Experiments suggest that, when γ_I is low, $\eta \approx 1$. When γ_I is moderate, the BER with interference canceling algorithms outperforms TIN substantially, but is still much higher than the expected value if $\eta = 0$. Finally, when γ_I is very high, there exists some residual BER floor wall due to the inability of the receiver to fully remove interference. To calibrate the parameter $0 < \eta < 1$ we assume a best case scenario where a MMSE estimation of the interferece is obtained and substracted. The relation between mutual information and MMSE in an AWGN channel[30] establishes that $\eta \geq \frac{\partial \text{I}(\mathbf{a}_n^{(1)};\mathbf{r})}{\partial \gamma}$, where $\mathbf{a}_1$ denotes the first interference and $\mathbf{r}_n$ the received samples during bit b_n. As the exact evaluation of this mutual information with non-Gaussian signals can be challenging, we verified in our experiments that a reasonable approximation of the BER can be achieved by approximating the signals as Gaussians for the purpose of computing the calibration term $\eta \simeq \frac{\partial}{\partial \gamma_I} \log(1 + \gamma_I) = \frac{1}{1+\gamma_I}$. Therefore the final calibration value is set as

$$\eta = \begin{cases} 1, & \gamma_I \leq 1, \\ \frac{1}{P_I^{\pi(1)}(1+\gamma_I)}, & 1 \leq \gamma_I < \frac{1}{\eta_{\min}} - 1, \\ \frac{\eta_{\min}}{P_I^{\pi(1)}}, & \gamma_I \geq \frac{1}{\eta_{\min}} - 1, \end{cases} \tag{12}$$

with $\eta_{\min} = 1$ for TIN and $\eta_{\min} < 1$ for any interference canceling receivers we wish to evaluate. As we have seen, satellite scenarios are unlikely to benefit from the DO-260B multi-sample technique, but the optimal MAP receiver or even SIC techniques as proposed in[31] can all be modeled in our physical layer abstraction with careful calibration of this value.

4 | BEAMFORMING

This section aims to propose and analyze beamforming strategies to enhance the probability of aircraft detection. Unlike most existing studies [18,19,20], our approach does not focus on global blind optimization. Instead, we first characterize the interference environment and, based on the resulting insights, identify suitable beamforming technique candidates. Specifically, we discuss amplitude tapering to reduce sidelobe levels, null-steering to reduce interference coming from specific locations, sparse apertures to improve spatial resolution and beam diversity.

4.1 | Interference characterization

To evaluate the interference mechanisms in the ADS-B reception, we resort to a baseline beam layout based on a uniform hexagonal grid of beams with beams crossover at -3 dB, so ensuring that all aircraft fall within the main lobe of at least one beam. The angular beam separation (ABS) between beam centers in the UV angular coordinates is given by

$$ABS = \sqrt{3}\sin\frac{HPBW}{2}, \tag{13}$$

where $HPBW$ is the half-power beamwidth of the satellite antenna. The target FoV considers as potentially visible aircraft those located on a satellite footprint delimited by the region in which the satellite is seen at an elevation of 0°. For an orbit altitude of 550 km it yields to a maximum satellite tilt angle (with respect to nadir) of 67°. Therefore, to improve coverage at the FoV edges, the hexagonal grid includes the satellite beam centers with tilt angle up to θ_s <= 70°, We use a conventional beamformer so for the beam b, it is just the steering vector to the beam center angular position derived by the grid, thus

$$w_b^H = \frac{1}{\sqrt{N}} e^{j\frac{2\pi]}{\lambda}(xu_k + yv_k)}. \tag{14}$$

For the 8x8 antenna with half-wavelength spacings, the $HPBW$ at nadir is 12.6°, so this baseline beam layout results in 97 beams.

The scenario for evaluation considers an aircraft distribution captured on the first of June of 2025. The satellite is assumed to follow a quasi-polar orbit, with an inclination of 87°. At the start of the simulation window (i.e. t = 0 s), which spans for 8 s for the evaluation of the $PUI(8)$, the satellite is located at 40.7° latitude, -77° longitude, just over U.S. East Coast. This constitutes a highly challenging scenario, with 6,937 aircraft within the FoV, while still exhibiting significant diversity: oceanic regions with low aircraft density, the Gulf of Mexico and the U.S. inland areas with moderate densities, and the East Coast characterized by very high aircraft density. Fig. 5 compares the aircraft distribution in geodetic coordinates and in UV coordinates centered at the satellite antenna. On top of the distribution, Fig. 5b illustrates the maximum SNR at which each aircraft is received across the beam layout (color scale) when only considering top-mounted antenna transmissions. It also shows the aircraft presenting $PUI(8)$ < 95% (red dots), evaluated using the TIN detector model following the procedure detailed in Section 5. Fig. 6 shows the aircraft distribution and corresponding SNR when considering transmissions from both top and bottom antennas and at the to ends of the simulation window (i.e. t = 0 s and t = 8 s).

Fig.5 and 6 allow deriving meaningful insights. First, although the aircraft distribution in geodetic coordinates is highly heterogeneous, its projection onto the antenna FoV concentrates aircraft toward its edges due to the Earth's curvature, leading to high projected aircraft densities, particularly beyond 60°. For instance, in the considered scenario, the maximum aircraft density in geodetic coordinates is observed along the U.S. East Coast, whereas, in the antenna UV plane, the highest aircraft concentration occurs near the western edge of the coverage area, where a large fraction of the aircraft flying over the continental U.S. are projected. This effect poses a significant challenge to extending the effective coverage in the considered scenario, as confirmed by the fact that most aircraft with $PUI(8)$ < 95% are in the θ_s > 54° region. We emphasize that the specific aircraft density distribution and, consequently, the location of the most challenging region are scenario dependent. Nevertheless, the projection induced by the Earth's curvature may result in high aircraft concentrations near the FoV edge when sufficiently dense traffic spanning all over the coverage area is present. Further examples of this effect are provided by the alternative scenarios evaluated in Section V and depicted in Figs. 15 and 16. Second, when considering only transmissions from top-mounted antennas (see Fig. 5b), a low-SNR ring is observed for 20° < θ_s < 30°, corresponding to the dip in the aircraft antenna radiation pattern depicted in Fig. 2. This phenomenon has a tangible impact on system performance, as evidenced by a few aircraft exhibiting $PUI(8)$ < 95% within this region. Again, this effect is scenario dependent. However, aircraft equipped with

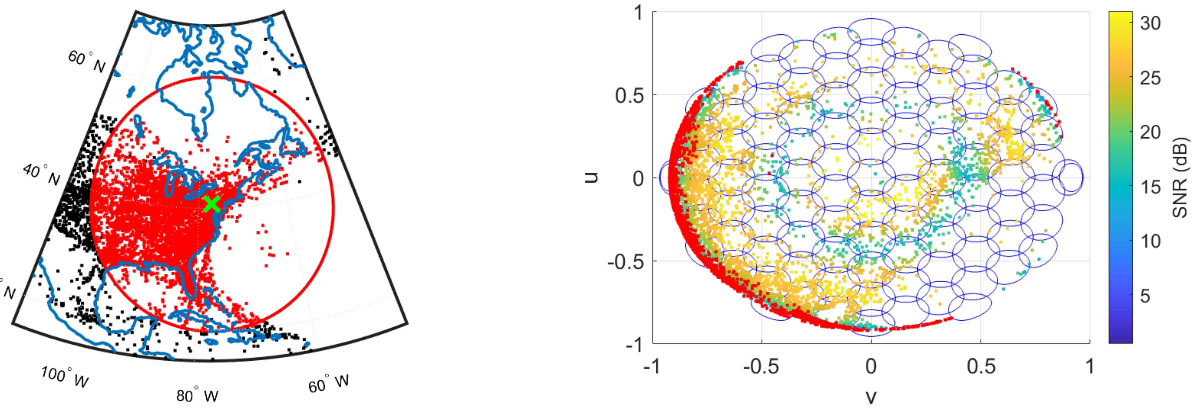

(a) (b)

FIGURE 5 Aircraft distribution in geodetic (a) and uv (b) coordinates. Green cross on subfigure (a) depicts the satellite position. In subfigure (b), red dots illustrate aircraft with $PUI(8) < 95\%$, and color scaled dots the SNR received from top antenna transmissions of each aircraft.

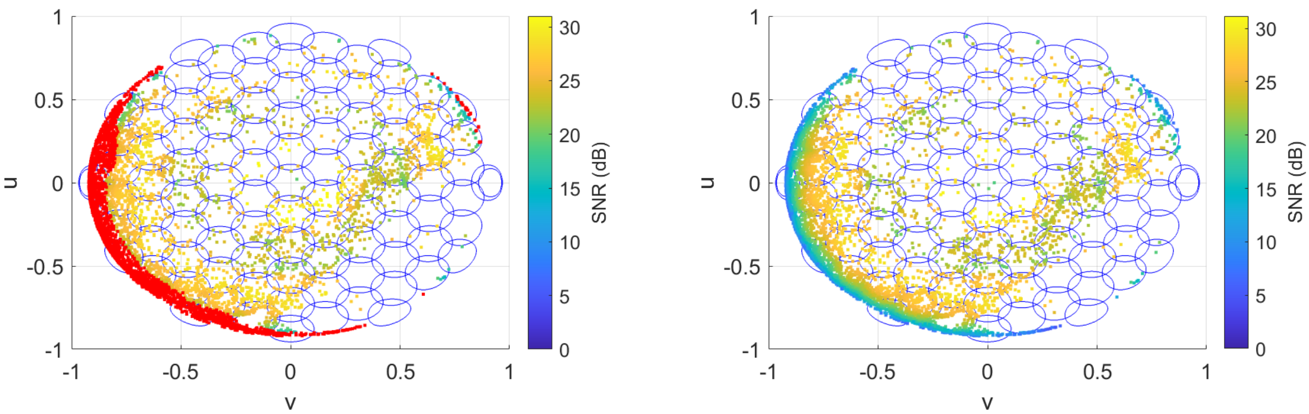

(a) (b)

FIGURE 6 Aircraft distribution in uv coordinates at $t = 0$ s (a) and $t = 8$ s (b). Color-scaled dots indicate the highest SNR received from each aircraft through either the top or bottom antenna; and red dots in subfigure (a) aircraft with $PUI(8) < 95\%$.

antennas exhibiting the assumed radiation pattern and located within this ring will experience lower SNR levels, making them more vulnerable to potential interferers. When transmissions from both the top and bottom antennas are considered (see Fig. 6), the resulting antenna diversity largely mitigates the low-SNR ring region. This represents the main benefit of considering transmissions from both antennas. However, the increased message load also leads to higher interference levels, increasing the number of aircraft with $PUI(8) < 95\%$ near the coverage edge. Finally, Fig. 6 shows that, although the relative aircraft positions and corresponding SNRs vary within an 8s window, the aggregate aircraft distribution evolves at a much slower rate. This behavior favors adaptive beamforming solutions based on the aggregate traffic distribution rather than on the instantaneous positions of individual aircraft. In view of this, for the remainder of this section the aircraft spatial distribution and beam layout are evaluated from a representative aircraft snapshot, which remains fixed during the 8 s observation window. Aircraft and satellite movement are taken into account in the system evaluations of Section 5.

To further assess the impact of signal collisions, we evaluate the number of potential single interferers for each aircraft. From (4), single-interferer candidates can be identified as those satisfying

$$\mathrm{SNR}_{bc} \geq \frac{SNR_{bn}}{SINR_{min}} - 1, \tag{15}$$

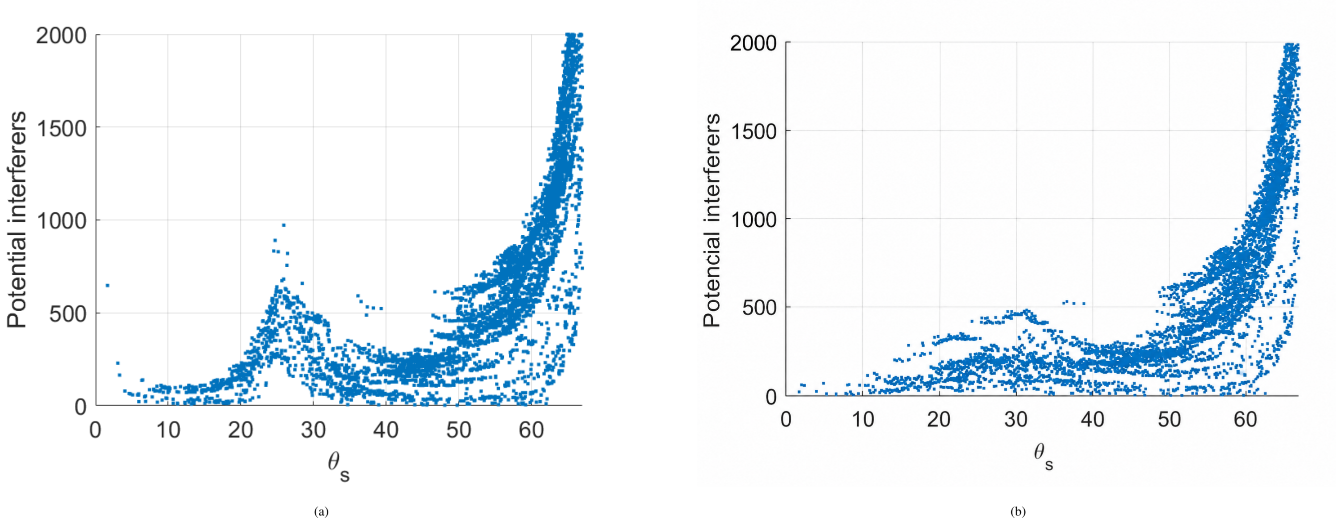

FIGURE 7 Number of potential single-interferers as a function of θ_s considering only top antenna transmissions (a) or both top and bottom (b).

where index c refers to interfering candidates and index n to the aircraft under evaluation. For the TIN detector model, the minimum SNR required to achieve $PUI(8) < 95\%$ can be calculated by inverting expressions (5) and (11), which results in a minimum SNR of $SNR_{min} = 7.3$ dB. Fig. 7 illustrates the number of potential interfering candidates for each aircraft as a function of the aircraft angular position (θ_s) considering either only transmissions from top-mounted antennas or from both. For the latter case we consider the best SNR from any of the two antennas for both the aircraft under evaluation and the potential interferers. In both cases, the number of potential interferers increases for $\theta_s > 50°$, with an exponential growth beyond $\theta_s > 60°$. Moreover, for only top transmissions, a large increase is also observed in the region $20° < \theta_s < 30°$, corresponding to the low-SNR ring, which is partially mitigated when considering antenna diversity. Consequently, the probability of collisions correlates not only with aircraft density but also with low SNR levels, with the combination of both effects leading to the worst-case scenarios. The underlying reason is that aircraft received with lower SNR can be potentially interfered by a larger number of other aircraft, including those not located within the same antenna main lobe but received through sidelobes.

Fig. 8 further highlights this issue by showing the distribution of potential interferers for two representative aircraft (one located within the low-SNR ring and the other near the edge of the coverage area) considering top-antenna transmissions only. Although antenna sidelobes may provide some degree of beam diversity, they have a clear detrimental impact on aircraft operating at low SNR when, as in the scenarios considered herein, high aircraft densities populate the sidelobe regions.

4.2 | Amplitude tapering

The number of potential interfers for each aircraft, especially for those at low-SNR regions, can be reduced by lowering the beam sidelobes. A well-known approach is to apply amplitude tapering across the receiving aperture[32,33]. Without loss of generality, we focus here on a Taylor window taper, which enables a direct evaluation of the trade-off between sidelobe levels (SLL) and main-lobe beamwidth (*i.e.*, lower targeted SLLs result in wider main beams). In particular, we consider the synthesis of beams with four nearly constant sidelobes and a maximum sidelobe level below SLL_{max}.

4.3 | Null-steering

Null-steering is commonly used to mitigate interference; however, in ADS-B reception, where transmissions occur at random times, it is not straightforward to determine the optimal null directions. Given that sidelobes are already controlled via amplitude tapering, a practical strategy is to place nulls in the vicinity of the main beam, where aircraft density and potential interference are typically highest. Nevertheless, null-steering inherently widens the main beam and increases other sidelobes, limiting its overall effectiveness. Fig. 9 exemplifies this limitations. Fig. 9a depicts the received SNR and detected aircraft for a single beam in the baseline layout. Large SNR values are observed not only within the -3 dB main-beam contour but also in its

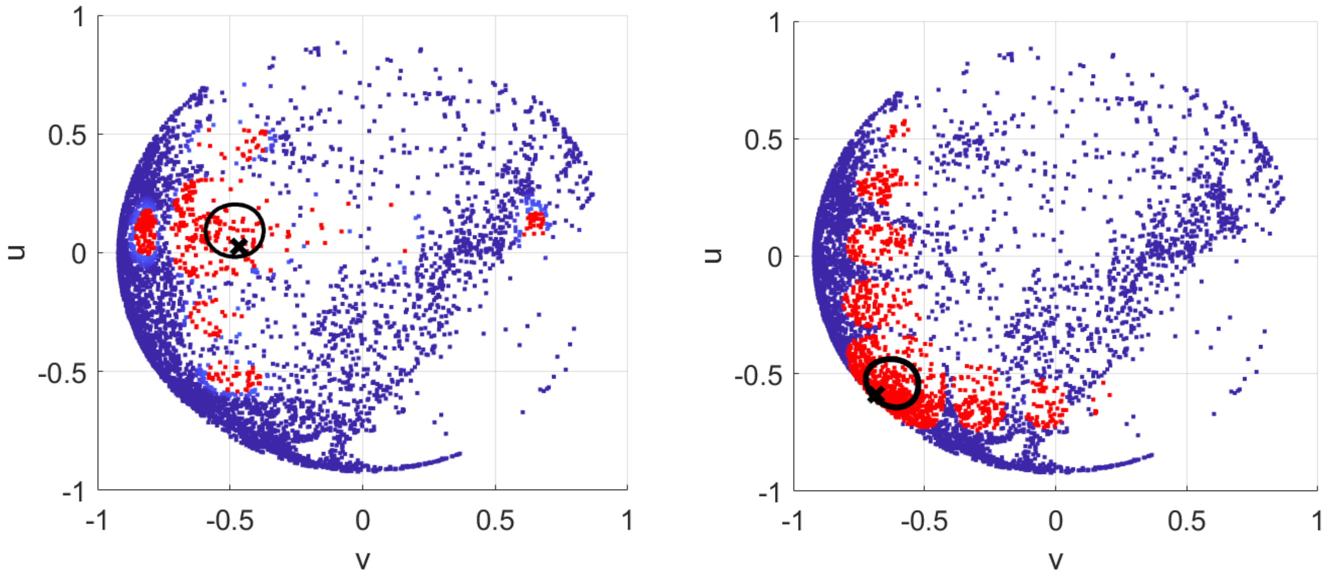

(a) (b)

FIGURE 8 Distibution of potential single-interferers considering only top antenna transmissions for an aircraft at the low-SNR ring (a) and at the FoV edge (b). Red dots identify potential interferers, black crosses the aircraft under evaluation, and black circles the -3 dB contour of beam under consideration.

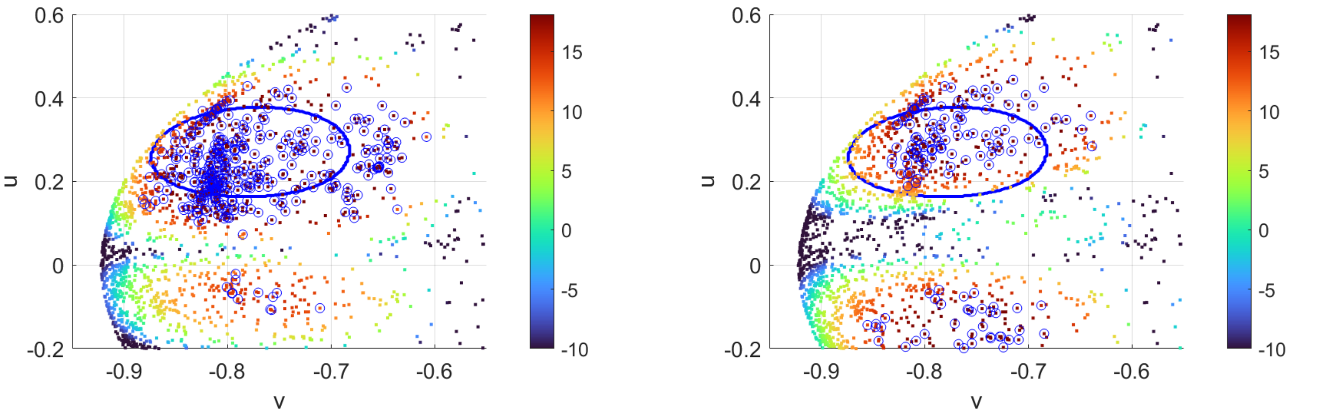

(a) (b)

FIGURE 9 Detection map for a given beam at coverage edge: (a) baseline beam, (b) beam with nulls at uv_{nulls} = ([0.04, 0.83], [0.25, 0.5], [0.1, 0.83], [0.5, 0.58]). Blue circles depict detected (i.e. $PUI(8) \geq 95\%$) aircraft and colored dots non-detected aircraft according to their SNR levels. Big blue circle depicts the -3 dB contour of the baseline beam.

immediate surroundings and in the first sidelobe. As a result, aircraft are detected both in the sidelobe and near the main beam, yet a significant number of missed detections still occur within the main beam itself. In Fig. 9b, four nulls are synthesized at uv_{nulls} = ([0.04, 0.83], [0.25, 0.5], [0.1, 0.83], [0.5, 0.58]) using a Linearly-Constrained Minimum Variance (LCMV) beamformer[34]. While the SNR is effectively reduced in the targeted regions, eliminating detections there and slightly affecting the adjacent main-beam area, this does not improve detection elsewhere in the main beam. In fact, the main-beam SNR is slightly reduced, whereas the first sidelobe SNR increases.

The conclusion is that achieving robust interference suppression would require full pattern synthesis, generating broad nulls near the main beam while controlling beam widening in low-density regions. However, such an approach demands computationally intensive pattern optimization, which we aim to avoid in this work.

4.4 | Distributed sparse array

Reducing the number of potential interferers in the vicinity of the main beam requires increasing the array spatial resolution, which is inherently limited by the aperture size. Distributed sparse arrays can enhance resolution while maintaining the same number of radiating elements; however, such architectures are incompatible with the constrained real-space available for antenna deployment considered here. A practical alternative is to split the original $1m^2$ array into several subarrays and distribute them across the satellite platform while preserving the same overall occupied area. As a matter of example, we repeated the analysis of Fig. 9 using a configuration of four subarrays, each composed of 4x4 elements, randomly distributed within a $2m^2$ area. Randomization is employed to mitigate grating lobes, although four subarrays alone do not achieve sufficient suppression. Fig. 10 illustrates the resulting subarray configuration, while Fig. 11 shows the corresponding detection map and radiation pattern. This configuration clearly reduces the main beamwidth; however, nearby grating lobes still illuminate a significant number of potential interferers. Further distribution of elements would allow reducing the grating lobes but this will effectively increase the area occupied on the satellite platform.

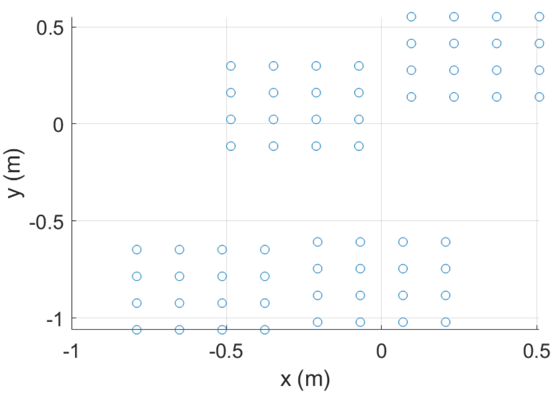

FIGURE 10 Position of radiating elements for the distributed and randomized antenna array

4.5 | Beam diversity: over and under sampling

Based on the previous results, we propose a solution that combines amplitude tapering with beam diversity. The core idea is to increase the beam density in regions with high aircraft density by oversampling these areas relative to the baseline beam grid with –3 dB beam crossovers. This oversampling results in significant beam overlap, allowing a single aircraft to be simultaneously detected by multiple beams. Since each aircraft experiences a different set of potential interferers in each beam, the overall probability of detection is effectively increased. Additionally, oversampling near the edges of the FoV provides a more uniform and increased SNR levels in these regions. Since beam oversampling rapidly increases the total number of beams, it should be applied only in regions with high aircraft density and complemented with undersampling in areas of low density. Our proposed approach to implement over- and undersampling maintains the baseline hexagonal beam grid while adjusting the angular spacing between beams according to

$$ABS = \sqrt{3} \sin \frac{HPBW}{2 \cdot BoF}, \quad (16)$$

where BoF is a beam overlapping factor. Note that BoF=1 corresponds to the baseline case, with a beam crossover level of–3 dB.

To identify the regions where over/under sampling should be applied without resorting to a full simulation requiring the message generation and the SINR computation at bit level, we propose a three-stage process. It assumes that the message transmissions follow a Poisson distribution with a rate of $N\lambda$, being N the number of potential interferers and λ the message rate. Then the probability of having no collisions reads as

$$Pd_{nc} = e^{-N\lambda 2L}, \quad (17)$$

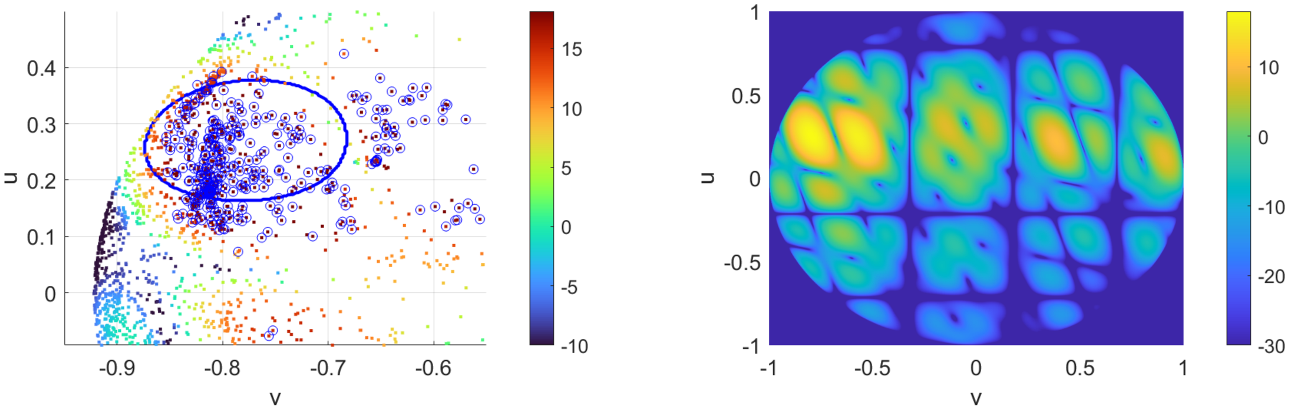

(a) (b)

FIGURE 11 Detection map (a) and radiation pattern (b) for the antenna architecture in Fig. 10. In subfigure a) blue circles depict detected (i.e. $PUI(8) \geq 95\%$) aircraft and colored dots non-detected aircraft according to their SNR levels. Big blue circle depicts the -3 dB contour of the baseline beam.

where L is the message length. The three steps are the following:

- **Stage 1: Selection of undersampling beams:** We generate a reference undersampling layout with BoF = 0.5 and Taylor tapering with SLL_{max}=-80 dB to increase beamwidth. For each aircraft and beam, we compute the number of potential single interferers using (15), and substitute N in (17) to obtain the probability of no collision for that aircraft and beam. We assume it as the probability of successful detection and apply (5) and (6) to estimate the $PUI(8)$. Then, we assign each aircraft to a given beam based on maximum SNR criteria, and we select the beams for which all assigned aircraft present $PUI(8) \geq 0.95$. Let the number of selected beams be B_1.
- **Stage 2: Selection of normal sampling beams:** We generate a reference layout with BoF = 1 and Taylor tapering with SLL_{max}=-20 dB, and discard the aircraft assigned to the selected beams in Stage 1. Then we repeat the process in Stage 1 that yields to the selection of B_2 beams. Note that beams without any assigned aircraft are discarded.
- **Stage 3: Selection of oversampling beams:** We discard the aircraft already assigned in previous stages. Then, assuming that the total number of beams is limited to B, we calculate the number of oversampling beams as $B_3 = B - B_1 - B_2$. Then we optimize the oversampling factor BoF so that the number of oversampling beams with assigned aircraft is B_3

This process use hard assumptions like only considering single interferers, a Poisson distribution of messages, a probability of detection based on a single collision and equal power transmissions for all aircraft. Still it provides a good approximation of candidate regions for under and over sampling, as demonstrated in Section 5.2.

In practice, the geometry of a LEO satellite evolves continuously, causing the instantaneous SNR and SINR experienced by each aircraft to vary over time. However, the proposed technique does not depend on the exact aircraft positions, but rather on their aggregated spatial distribution, which typically varies slowly over short time intervals, such as the 8 s window used to evaluate the PUI, as exemplified in Fig. 6. Consequently, a practical system would only need to update the beamforming weights at a relatively low rate to track changes in the relative aircraft distribution. Moreover, aircraft spatial distributions are largely predictable for a given region, date, and time of day, enabling beam layouts to be computed in advance.

4.6 | Three-dimensional antenna

For the sake of completeness, let us point out that from a theoretical perspective, the gain and beamwidth at the coverage edge can be improved by using inclined antenna panels. However, achieving full 360° azimuth coverage requires multiple panels or a conical configuration[35,36], which reduces the number of elements effectively illuminating a given region and increases the antenna profile, complicating integration within the satellite platform. A fair comparison between planar and three-dimensional panel configurations is not straightforward, as it is difficult to maintain the same antenna surface area or number of radiating elements. Therefore, this analysis is left for future studies.

5 | SYSTEM EVALUATION

5.1 | Methodology

An in-house simulator has been developed to perform both the preliminary assessment described in the previous section and the extended system evaluation presented in the following subsection. The simulator consists of two modules: the channel generator and the traffic generator. The channel generator performs the following steps: (i) imports the aircraft distributions in geodetic coordinates; (ii) identifies aircraft in the FoV as those presenting $\theta_a \geq 0°$, which at 550km corresponds to a satellite tilt angle of θ_s = 67°; (iii) defines the satellite position; (iv) models the system geometry; and (v) applies (2) and (3) to calculate a *BxN* matrix of SNR_{bn} coefficients, according to a given beam layout, for both top and bottom antenna transmissions. The aircraft distributions are imported from ADSBexchange[37]. Since ADS-B Exchange provides aircraft position data at 10 s intervals, two consecutive datasets are imported and interpolated to generate aircraft position snapshots every 0.5 s. The built-in MATLAB SGP4 orbital propagator is used to compute the satellite position at the same temporal resolution. The channel generator then outputs two SNR matrices of dimensions $B \times N \times T_s$, where B, N, and T_s denote the number of beams, aircraft, and time snapshots, respectively. The two matrices correspond to transmissions from the top and bottom aircraft antennas.

The traffic generator (i) models ADS-B message generation for all aircraft; (ii) randomly assigns the available transmit power to each aircraft according to the distribution in Table 1, and rescales the SNR matrix accordingly; and (iii) applies (4),(11),(5) and(6) to compute the overall PUI(8) for each aircraft.

The simulation window is set to 8 s corresponding to the transmission of 8 intended ADS-B position messages through each antenna. The transmission instants of these position messages are generated using random inter-arrival times built from the sum of two uniform components. Each of these components is uniformly distributed in the range $[0.4, 0.6]$ seconds relative to the previous message, which introduces controlled variability around a nominal update interval while avoiding overly deterministic patterns. A random initial offset is also added so that transmissions are not aligned across aircraft. From these baseline position messages, two additional ADS-B message streams are derived for each antenna. These are generated by adding independent random offsets to each position message, effectively creating delayed replicas that represent different ADS-B squitter types. The offsets are drawn from distinct ranges, ensuring temporal separation between the message types while preserving correlation with the original position message timing. Finally, Mode-S messages are generated differently to reflect their asynchronous nature. For each position message interval, multiple Mode-S replies are placed by taking the integer part of the position timestamp (i.e., aligning to a coarse time grid) and adding uniformly distributed random offsets within that interval. This produces several independent transmissions per second that are not tightly synchronized with ADS-B messages. Mode-S messages are transmitted through the top antenna in the scenario considering top-antenna transmissions only, whereas they are randomly assigned to either the top or bottom antenna when transmissions from both antennas are considered. After generating all message types, the algorithm enforces a minimum time separation between transmissions of the same aircraft (equal to the message duration), ensuring that no self-overlapping occurs.

Once all message timestamps are generated for every aircraft and message type, they are merged into a single global timeline. This is done by concatenating all transmissions and sorting them in time, while keeping track of the originating aircraft for each message. To identify potential collisions, the algorithm scans this sorted timeline and, for each position message, dynamically defines a time window of vulnerability equal to the message duration before and after its transmission time. Using a sliding window approach, it efficiently selects all candidate interfering messages whose transmission intervals overlap with the message of interest. Once the set of interfering messages is identified, the algorithm evaluates interference at the bit level. For each bit of the desired message, it determines which interferers overlap in time and constructs an interference matrix. Them it applies (11),(5) and (6) to calculate the PUI(8). For each message, the SINR values are taken from the closest snapshot. Let us remark that for the PUI(8), we consider position messages as desired messages, whereas interfering messages include any ADS-B or Mode-S message from other aircraft.

The simulation is carried out in a Monte Carlo fashion, with each realization considering a different random traffic generation and a different distribution of the aircraft transmit powers. The results are averaged across all realizations.

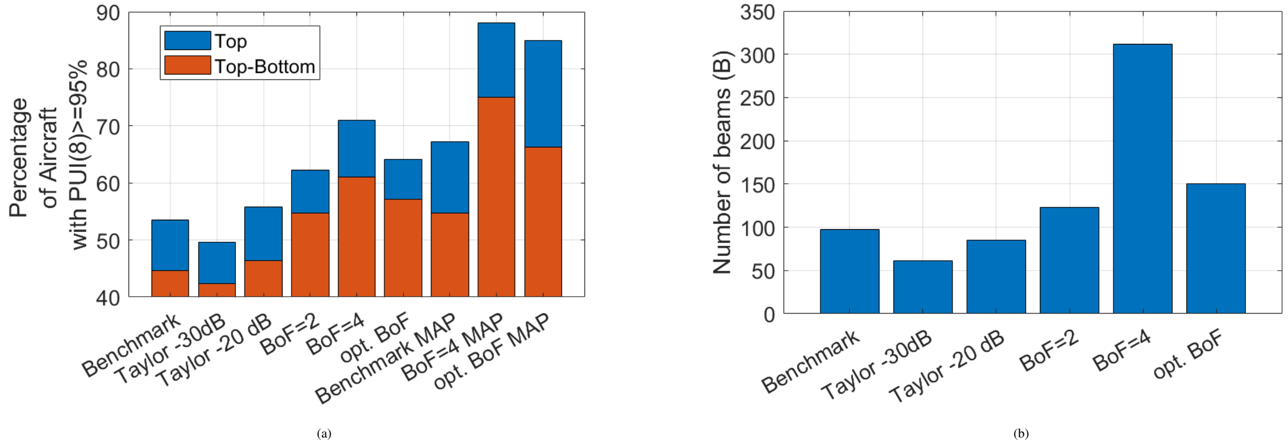

FIGURE 12 Comparison of the different proposed schemes: (a) percentage of aircraft satisfying $PUI(8) \geq 95\%$ considering either only transmissions from top antenna or both top and bottom; (b) number of beams for each scheme.

5.2 | Numerical results

The scenario under evaluation is the same as in Section 4.1, featuring a satellite pass over the U.S. East coast with 6,937 aircraft in the satellite FoV during the simulation window. The following beam layouts are compared:

- Baseline layout (no tapering and BoF=1)
- Taylor tapering layout with SLL_{max}=-30 dB, BoF=1
- Taylor tapering layout with SLL_{max}=-20 dB, BoF=1
- Taylor tapering layout with SLL_{max}=-20 dB, BoF=1 as a baseline and BoF=2 for $\theta > 50°$ and $155° < \phi < 320°$
- Taylor tapering layout with SLL_{max}=-20 dB, BoF=1 as a baseline and BoF=4 for $\theta > 50°$ and $155° < \phi < 320°$
- Taylor tapering layout with SLL_{max}=-20 dB and optimized BoF using the three-stage process described in Section 4.5 with a maximum of B = 150 beams

Fig. 12 provides a numerical comparison of the considered beam layouts in combination with TIN and MAP decoders by reporting the percentage of aircraft within the FoV presenting $PUI(8) \geq 95\%$ and the total number of beams used in each case. In addition, Figs.13 illustrates the percentage of aircraft with $PUI(8) \geq 95\%$ as a function of the scan angle from nadir. This evaluation relies on a sliding window of 1° to average the number of detected and present aircraft for each tilt angle value. It enables the assessment of the effective coverage, defined here as the angular region in which the percentage of aircraft with $PUI(8) \geq 95\%$ exceeds 99%.

We first compare the two traffic models, considering either top-antenna transmissions only or transmissions from both the top and bottom antennas. Although both models exhibit similar qualitative trends across the different beamforming schemes, several notable differences arise. First, considering top-antenna transmissions only consistently results in a larger percentage of aircraft achieving $PUI(8) \geq 95\%$, suggesting that the increased traffic load associated with transmissions from both antennas outweighs the corresponding diversity benefits. Accordingly, the top-antenna-only model also yields a larger effective coverage area, consistent with its lower traffic load. Finally, when only top-antenna transmissions are considered, some aircraft within the low-SNR ring around $\theta_s = 30°$ exhibit $PUI(8) < 95\%$ with the benchmark beam layout. This degradation is mitigated by the tapered solutions. When transmissions from both the top and bottom antennas are considered, the resulting antenna diversity already mitigates this effect without requiring tapering. These results highlight the need of accurately modeling the radiation patterns of antennas mounted on the aircrafts.

Let us now focus on the model considering both top and bottom antenna transmissions. The rationale behind the selected comparison schemes is as follows. The baseline layout described in Section 4.1 is used as a benchmark, as it does not apply amplitude tapering nor beam oversampling and considers the TIN detector, which is optimal under an AWGN channel. We then compare two Taylor amplitude tapering solutions with SLL_{max} = –20dB and SLL_{max} = –30dB, which show different performance at the coverage edge. Indeed, amplitude tapering increases the beamwidth, resulting in a reduced number of beams,

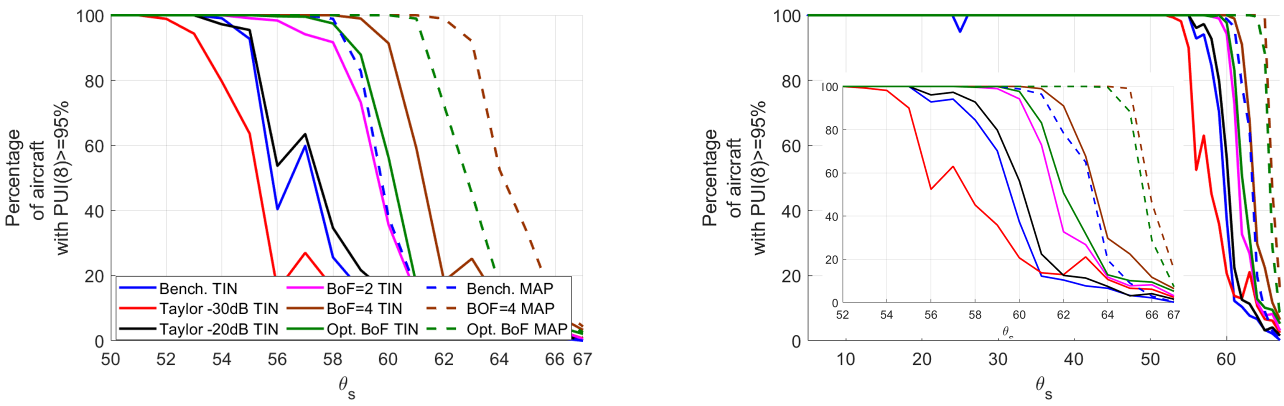

(a) (b)

FIGURE 13 Percentage of aircraft satisfying $PUI(8) \geq 95\%$) as a function of tilt angle from Nadir: (a) Transmissions from both top and bottom antennas (b) Transmissions only from top antennas (inset showing zoom to $\theta_s > 52°$).

which in the case of Taylor tapering with SLL_{max} = –30dB leads to degraded coverage at the FoV edges and, consequently, to $PUI(8)$ values worse than those obtained with the benchmark. By contrast, Taylor tapering with SLL_{max} = –20dB slightly enlarges the effective coverage. In terms of the percentage of aircraft over the total number within the FoV, Fig. 12 shows that Taylor tapering with SLL_{max} = –20dB achieves a slight improvement around 4%, together with a 37% reduction in the number of beams compared to the benchmark. Therefore, this scheme is adopted as the baseline for assessing beam diversity solutions.

In view of these results, we assess the impact of beam oversampling with $BoF = 2$ or $BoF = 4$ in the $\theta > 50°$ and $155° < \phi < 320°$ region. These regions are manually delimited based on the observation of failed detection distributions for the Taylor tapering with SLL_{max} = –20dB case. A significant performance gain over the benchmark layout is achieved. Specifically, a 37% increase in the total percentage of detected aircraft is obtained for $BoF = 4$, albeit at the cost of almost tripling the number of beams. In addition, the effective coverage is extended from 53° in the benchmark case to 59° for $BoF = 4$. However, practical systems may limit the number of beams that can be processed in parallel. To illustrate this, we perform the proposed layout optimization considering both over and undersampling with a maximum number of beams limited to 150 beams. Fig.14 illustrates the resulting optimized layout and the corresponding distribution of aircraft with $PUI(8) < 95\%$. It still provides and improvement of 28% on aircraft presenting $PUI(8) \geq 95\%$ with respect to benchmark while using just half the number of beams with respect to the $BoF = 4$ scheme.

Repeating the analysis with the MAP decoder highlights the benefits of employing a decoder capable of handling at least one strong collision. In particular, for the same beam layout, the improvement on the number of aircraft with $PUI(8) \geq 95\%$ over the TIN receiver is in the range of 22-30%. Furthermore, combining MAP with the optimized layout limited to 150 beams provides an improvement of 49% with respect to benchmark layout with TIN decoder. Such improvement is mainly devoted to the enlarged effective coverage that reaches up to 61°.

The proposed three-stage process for beam layout design with a limit of 150 beams is further assessed using two alternative scenarios. In both cases, an orbit with 87° of inclination is assumed. In Scenario 1, the satellite at $t = 0$ s is located at 38° latitude, -95° longitude, so around a central point inside U.S. This leads to a total of 9400 aircraft within the field of view. In Scenario 2, the satellite at $t = 0$ s is at 48° latitude, 10° longitude, so around a central point inside Western Europe. In this case, the total number of aircraft within the FoV is reduced to 4344. Fig.15 illustrates the scenarios in geodetic coordinates. Fig.16 depicts the resulting optimized layout and the corresponding distribution of aircraft with $PUI(8) < 95\%$ for both scenarios and the TIN decoder when considering transmissions from top and bottom antennas. As expected, oversampling is applied near the FoV edges where high aircraft density is present. Table 2 summarizes the numerical results comparing these layouts with the benchmark for both TIN and MAP decoder. Although the absolute percentages of detected aircraft and effective coverage depend on aircraft densities, an improvement with respect to benchmark is obtained applying the optimized layout, and further enlarged when considering also the MAP decoder, confirming the results from the original scenario. These improvements also translate into larger effective coverage areas. For instance, when transmissions from both the top and bottom antennas are considered, the optimized beam layout combined with the MAP decoder increases the percentage of aircraft achieving $PUI(8) \geq 95\%$ by 13.1% and 15.2% with respect to the benchmark layout combined with the TIN decoder

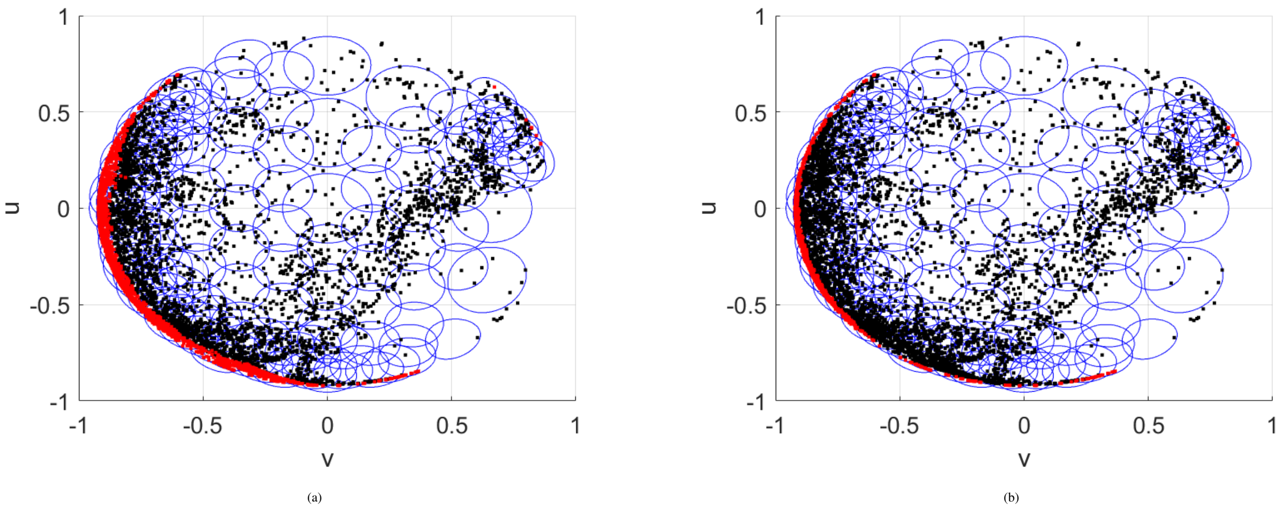

FIGURE 14 Optimized beam layout with a number of beams limited to 150 for TIN (a) and MAP (b) decoders. Blue circles show the -3 dB beam contours and red dots depict aircraft presenting *PUI*(8)<95%. Black dots correspond to aircraft with *PUI*(8) $\geq$ 95%.

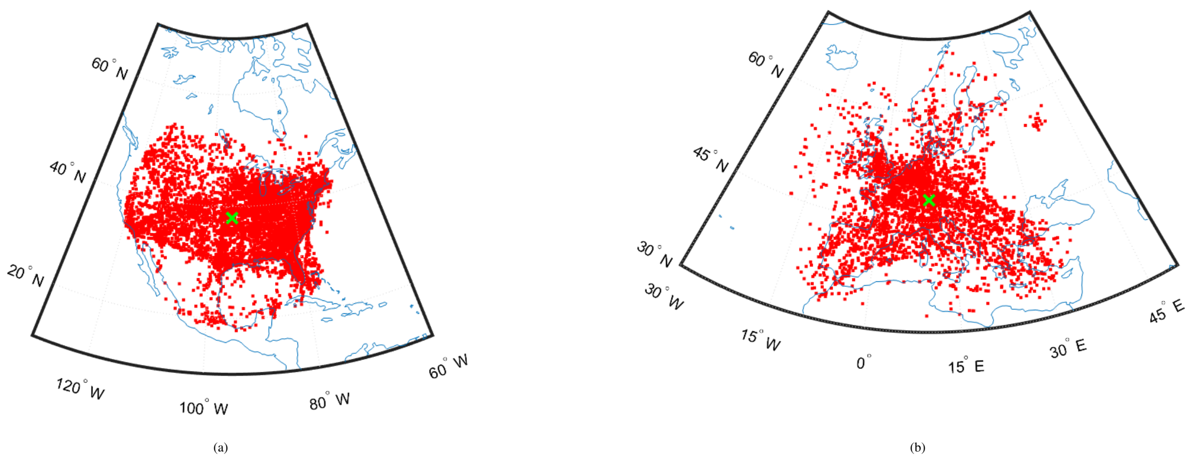

FIGURE 15 Aircraft distribution in geodetic coordinates for alternative scenarios 1 (a) and 2 (b). Green cross depicts the satellite position at t = 0 s.

in Alternative Scenarios 1 and 2, respectively. These improvements translate into an extension of the effective coverage by approximately 4° and 5°, respectively. These performance improvements are lower than those obtained for the original scenario for three main reasons. First, both alternative scenarios exhibit high aircraft densities along most of the coverage boundary, reducing the degree of spatial oversampling that can be achieved with the available 150 beams. Second, the overall aircraft density is significantly higher in Alternative Scenario 1, potentially requiring a larger number of beams to fully exploit the benefits of oversampling. Third, the benchmark beam layout already performs well in Alternative Scenario 2 due to the lower aircraft density, leaving less room for improvement. These results suggest that the limit of 150 simultaneous beams deserves further investigation, particularly regarding the tradeoff between payload complexity and effective coverage across different worst-case traffic scenarios. Nevertheless, the results consistently demonstrate that spatial oversampling provides a systematic improvement over the benchmark beam layout, highlighting its effectiveness as a practical beamforming strategy even under challenging traffic conditions.

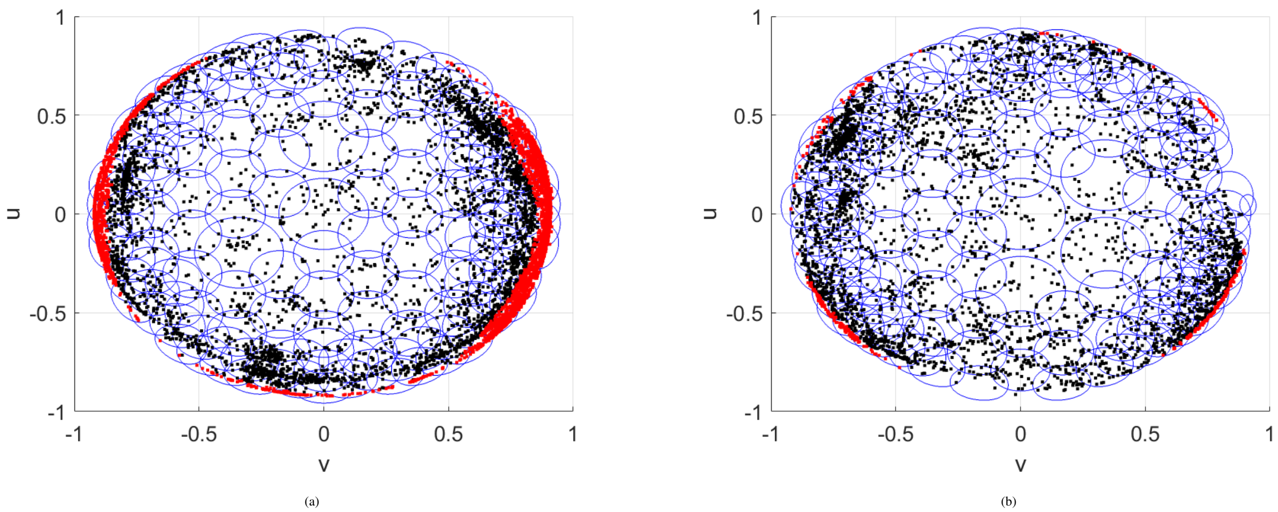

FIGURE 16 Results for optimized beam layouts with a number of beams limited to 150, TIN decoder and alternative scenarios 1 (a) and 2 (b). Blue circles show the -3 dB beam contours and red dots depict aircraft presenting $PUI(8)<95\%$. Black dots correspond to aircraft with $PUI(8) \geq 95\%$.

TABLE 2 Comparison of optimized layouts with $B = 150$ with benchmark layouts in terms of percentage of aircraft with $PUI(8) \geq 95\%$ and effective coverage

Layout	Scenario 1-TIN	Scenario 1-MAP	Scenario 2-TIN	Scenario 2-MAP
Benchmark Top	43.0% / 54°	49.8% / 58°	86.2% / 61°	91.7% / 64°
Optimized Top	51.2% / 58°	65.5% / 61°	94.6% / 65°	97.5% / 65°
Benchmark Top-Bottom	39.8% / 54°	43.3% / 55°	81.6% / 60°	86.8% / 62°
Optimized Top-Bottom	44.8% / 55°	51.6% / 58°	90.7% / 63°	94.0% / 65°

6 | CONCLUSIONS

This paper proposed an evaluation framework for next-generation space-based ADS-B systems characterized by larger antenna apertures and targeting global autonomous coverage. In contrast to existing literature, it enabled accurate interference modeling by accounting for heterogeneous interference levels arising from aircraft located at different positions. This modeling capability allowed an in-depth characterization of high-density aircraft environments, highlighting the detrimental impact of antenna sidelobe levels.

Based on these insights, a beamforming strategy combining amplitude tapering for sidelobe level containment, beam oversampling to exploit beam diversity gains in dense coverage-edge regions, and beam undersampling in sparse regions to limit the total number of beams was proposed and evaluated. A three-stage method leveraging on several assumptions was proposed to automatically generate optimized layouts applying over and under sampling in specific regions. The performance achieved by the resulting beam layouts largely depends on the traffic scenario and on the imposed limit on the total number of simultaneous beams Still, the proposed layouts provided consistent improvements over a uniform beam grid with -3 dB beam crossovers, both in terms of extended effective coverage and on the total number of aircraft satisfying a given update interval probability. These gains were significantly enhanced when the proposed beamforming strategies were combined with a MAP decoder capable of mitigating the impact of a single strong ADS-B or Mode-S collision. These results provide useful design insights for next-generation space-based ADS-B systems targeting standalone global coverage. In particular, they demonstrate the potential of increasing the effective coverage of each satellite through advanced digital beamforming, thereby enabling a reduction in constellation size at the expense of increased payload complexity. Future work should quantitatively investigate this tradeoff, including the relationship between onboard processing requirements, the number of simultaneous beams, effective coverage extension, and the resulting constellation size.

ACKNOWLEDGMENTS

The authors would like to thank Dr. Nader Alagha for the fruitful discussions that contributed to improve this study.

This work has been partially funded by the European Space Agency (ESA) as part of SATELLITE NETWORK OF EXPERTS V (4000130962/20/NL/NL/FE), under the Work Item 4.5: Receiver Front-end Architecture for Efficient Massive ADS-B Signal Detection; and by MICIU/AEI/10.13039/501100011033 FEDER/EU under projects PID2021-122483OA-I00 and PID2022-136512OB-C22. The views of the authors of this paper do not necessarily reflect the views of ESA.

REFERENCES

1. Airports Council International World . ACI World releases global airport traffic forecasts as long-term demand growth continues to reshape aviation. https://aci.aero/2026/01/28/aci-world-releases-global-airport-traffic-forecasts-as-long-term-demand-growth-continues-to-reshape-aviation/; 2026. Accessed: 2026-02-09.
2. Federal Aviation Administration . Title 14 of the Code of Federal Regulations (CFR), Part 91, Sections 91.225 and 91.227: ADS-B Out Equipment and Performance Requirements. https://federal.elaws.us/cfr/title14.part91.section91.225; 2024. Includes ADS-B Out equipage mandate as codified in U.S. law. Accessed 2026-02-09.
3. European Union Aviation Safety Agency . Regulation (EU) No 1207/2011 on Airspace Requirements ADS-B and Mode S Transponder Equipage. https://eur-lex.europa.eu/eli/reg_impl/2011/1207/oj/eng; 2011. Includes ADS-B Out and Mode S requirements within EU airspace. Accessed 2026-02-09.
4. Budroweit J, Eichstaedt F, Delovski T. Aircraft Surveillance From Space: The Future of Air Traffic Control?: Space-Based ADS-B, Status, Challenges and Opportunities. *IEEE Microwave Magazine.* 2024;25(12):68–76.
5. Garcia MA, Stafford J, Minnix J, Dolan J. Aireon space based ADS-B performance model. In: 2015:C2–1–C2–10. ISSN: 2155-4951
6. Garcia MA, Dolan J, Hoag A. Aireon's initial on-orbit performance analysis of space-based ADS-B. In: 2017:4A1–1–4A1–8
7. Baker KW. Space-Based ADS-B: Performance, Architecture and Market Options. Tech. Rep. SSC-ATS-P-091723, Summit Space Corporation; Centreville, VA, USA: 2023.
8. EUROCAE . Technical Specification for a 1090 MHz Extended Squitter ADS-B Surveillance System. *ED-129C.* 2022.
9. Reception of automatic dependent surveillance broadcast via satellite and compatibility studies with incumbent systems in the frequency band 1,087.7-1,092.3 MHz. *Report ITU-R M.2413-0.* 2017.
10. International Civil Aviation Organization . Annex 10 to the Convention on International Civil Aviation: Aeronautical Telecommunications, Volume IV – Surveillance and Collision Avoidance Systems. tech. rep., ICAO; Montreal, Canada: 2014. Available from https://www.icao.int.
11. Radio Technical Commission for Aeronautics (RTCA) . Minimum Operational Performance Standards for 1090 MHz Extended Squitter Automatic Dependent Surveillance–Broadcast (ADS-B) and Traffic Information Services–Broadcast (TIS-B). *RTCA DO-260B.* 2009.
12. Li K, Kang J, Ren H, Wu Q. A Reliable Separation Algorithm of ADS-B Signal Based on Time Domain. *IEEE Access.* 2021;9:88019-88026. doi: 10.1109/ACCESS.2021.3082077
13. Bi Y, Wu R, Jia Q. A high-precision and efficient algorithm for space-based ADS-B signal separation. *Journal of Navigation.* 2023;76(4-5):562–576. doi: 10.1017/S0373463323000139
14. Wang W, Zhao H. ADS-B overlapping signals separation based on minimum dispersion criterion. *Digital Signal Processing.* 2023;141:104172. doi: https://doi.org/10.1016/j.dsp.2023.104172
15. Wang W, Liu J, Liang J. Single antenna ADS-B overlapping signals separation based on deep learning. *Digital Signal Processing.* 2023;132:103804. doi: https://doi.org/10.1016/j.dsp.2022.103804
16. Li C, Bi Y. Independently Convolutional Gated Recurrent Neural Unit for Space-Based ADS-B Signal Separation with Single Antenna. *EURASIP Journal on Advances in Signal Processing.* 2023;2023(1):127. doi: 10.1186/s13634-023-01089-w
17. Bettray A, Litschke O, Baggen L. Multi-beam antenna for space-based ADS-B. In: IEEE 2013; Waltham, MA, USA:227–231
18. Yu S, Chen L, Li S, Zhang X. Adaptive Multi-beamforming for Space-based ADS-B. *Journal of Navigation.* 2019;72(2):359–374. doi: 10.1017/S0373463318000735
19. LI X, ZHANG X, TAN Y, MA J. Optimization of digital multi-beamforming for space-based ADS-B using distributed cooperative coevolution with an adaptive grouping strategy. *Chinese Journal of Aeronautics.* 2023;36(10):391-408. doi: https://doi.org/10.1016/j.cja.2023.03.008
20. Xiang Y, Li S, Chen L. Adaptive Beamforming for On-Orbit Satellite-Based ADS-B Based on FCNN. *Sensors.* 2024;24(21). doi: 10.3390/s24217065
21. Mosquera C, López-Valcarce R, Gómez-Cuba F, Artiga X, Henarejos P, Alagha N. Improved receiver architecture for efficient space-based massive ADS-B signal detection. *IET Conference Proceedings.* 2025;2025:33-40. doi: 10.1049/icp.2025.4032
22. Canlas J, Dolan J, Garcia MA. Update Interval Performance and Outlier Exclusion Methods for Aircraft Surveillance Systems. In: 2022:1-13
23. Proakis JG. *Digital Communications*. McGraw-Hill Series in Electrical and Computer EngineeringBoston: McGraw-Hill. 4. ed., [nachdr.] ed., 2007.
24. Le Neindre F, Dallet D, Ferre G, Boulanger E, Letellier F. An Enhanced Random Error CRC Correction for ADS-B Squitters Receivers. In: IEEE 2019; Belgrade, Serbia:1–4
25. *Aeronautical Telecommunications: International Standards and Recommended Practices. Volume IV, Surveillance Radar and Collision Avoidance Systems*. Montreal, Quebec, Canada: International Civil Aviation Organization. fifth edition ed., 2014.
26. Harman W, Gertz J, Kaminsky A. Techniques for improved reception of 1090 MHz ADS-B signals. In: . 2. IEEE 1998; Bellevue, WA, USA:G25/1–G25/9
27. Habibi Markani J, Amrhar A, Gagné JM, Landry RJ. NextGen ADS-B Software-Defined Reception with Enhanced Techniques. *Applied Sciences.* 2022;13(1):493. doi: 10.3390/app13010493
28. Jeffrey L. Gertz . Fundamentals of Mode S Parity Coding. Tech. Rep. Report ATC-117, MIT Lincoln Laboratory; .
29. Gómez-Cuba F, Lopez-Valcarce R, Mosquera C, Artiga X. ADS-B/Mode S Decoding: a Review and New Next-Gen MAP-Based Schemes. https://doi.org/10.5281/zenodo.21393003; 2026
30. Guo D, Shamai S, Verdu S. Mutual Information and Minimum Mean-Square Error in Gaussian Channels. *IEEE Transactions on Information Theory.* 2005;51(4):1261–1282. doi: 10.1109/TIT.2005.844072

31. Neindre FL, Ferre G, Dallet D, Letellier F, Pitois K. A Successive Interference Cancellation-based Receiver for Secondary Surveillance Radar. *IEEE Transactions on Aerospace and Electronic Systems.* 2022:1–12. doi: 10.1109/TAES.2022.3193649
32. Brookner E. *Practical Phased Array Antenna Systems*. Boston: Artech House, 1991.
33. Carrara WG, Majewski RM, Goodman RS. *Spotlight Synthetic Aperture Radar: Signal Processing Algorithms*. Boston: Artech House, 1995. Appendix D.2.
34. Sharma SK, Chatzinotas S, Grotz J, Ottersten B. 3D Beamforming for Spectral Coexistence of Satellite and Terrestrial Networks. In: 2015:1-5
35. Vera-Sánchez J, Martín-Nüñez , Ferrando-Rocher M, Ferrando-Bataller M. Circularly Polarized Conical Array for ADS-B Applications in LEO Satellites. In: 2025:1-3
36. Budroweit J, Drobczyk M. Design of a Small Size, Low Profile L-Band Antenna, Optimized for Space-Based ADS-B Signal Reception. In: IEEE 2018; Brisbane, QLD:1–6
37. ADSBexchange.com . ADS-B Exchange Unfiltered Global Flight Tracking. https://www.adsbexchange.com/; 2026. Accessed: Feb. 2026; worlds largest source of unfiltered ADSB flight data for research and tracking.

AUTHOR BIOGRAPHY

empty.pdf

Author Name. Please check with the journal's author guidelines whether author biographies are required. They are usually only included for review-type articles, and typically require photos and brief biographies for each author.